Integrated modeling of cracking during deep penetration laser welding of nickel alloys

M. Z. Gao, B. Mondal, T. A. Palmer, W. Zhang & T. DebRoy

I·M3
Institute of Materials, Minerals & Mining

Taylor & Francis
Taylor & Francis Group

RESEARCH ARTICLE

Check for updates

Integrated modeling of cracking during deep penetration laser welding of nickel alloys

M. Z. Gao[a], B. Mondal[b], T. A. Palmer [a,b], W. Zhang[c] and T. DebRoy[b]

[a]Department of Engineering Science and Mechanics, Pennsylvania State University, University Park, PA, USA; [b]Department of Materials Science and Engineering, Pennsylvania State University, University Park, PA, USA; [c]Department of Materials Science and Engineering, The Ohio State University, Columbus, OH, USA

ABSTRACT

During deep penetration laser welding of nickel alloys, interactions between composition and processing conditions can lead to the formation of defects. Inconel 740H, for example, has demonstrated a susceptibility to horizontal fusion zone cracking at locations between 70% and 80% of the weld depth during laser welding at powers above 5 kW. Coupling three-dimensional heat transfer, fluid flow, and stress modeling tools allowed that both the strain rate and stress normal to the solidification direction to be calculated. In the Inconel 740H welds, cracks formed at locations where the strain rate and stress simultaneously reached critical levels. No cracking was observed in the Inconel 690 welds, since the strain rate and stress did not simultaneously reach these critical levels.

Introduction

Solidification cracking is a commonly observed defect in welds made across a range of aluminium [1,2], steel [3,4], and nickel base alloys [5,6]. Cracks originate within the mushy zone along the trailing edge of the fusion zone when liquid films form along solidifying grain boundaries [2,6] and involve complex interactions between the alloy composition and the thermal and mechanical conditions driven by the welding process [7,8]. These complex interactions change with both alloy composition and processing conditions, leading to different dominant mechanisms that drive the cracking process. For example, the low strength of the liquid films combined with the stresses formed by the thermal and solidification shrinkage in the mushy zone leads to the formation of a crack [9]. In other cases, the remaining liquid within solidification structures and adjacent grains is insufficient to completely fill voids formed by thermal and solidification shrinkage [2].

The susceptibility to solidification cracking has largely been attributed to the alloy composition [2,6]. Changes in the alloying elements can impact elemental segregation, which, in turn, affects the solidification temperature range and the amount of liquid remaining in the mushy zone at the terminal stages of solidification [6]. A fraction of solid (f_s) value above 0.9 is typically considered to be most representative of the conditions at these terminal solidification stages that can lead to cracking [7,10]. In order to more accurately capture the alloying element segregation leading

to the formation of susceptible solidification structures during both additive manufacturing and welding processes, Scheil solidification models are commonly used [5,10]. Through these modeling approaches, the severity of the slope between the temperature gradient (dT) and the square root of the fraction solid $(f_s)^{1/2}$ can be captured and used as a criterion for predicting solidification cracking. Based on this general criterion, a steeper slope at the terminal stages of solidification indicates that the remaining liquid has a limited ability to flow between adjacent dendrites or grains, leading to a higher cracking susceptibility.

There is also a mechanical contribution to solidification cracking in which a tensile stress [9,11] is applied to the susceptible cracking region at a critical strain rate [9,12]. This mechanical contribution is codified through the Rappaz-Drezet-Gremaud (RDG) solidification cracking model [8]. Since these mechanical contributions are difficult to directly measure, their impact on solidification cracking is typically quantified using specialized experimental tools, such as Varestraint or transverse-motion weldability testing [5,6,13]. In these tests, the stress or strain rate that drives cracking is externally applied, and cracking susceptibility is then defined by a measurement of the crack length. However, these specialized tests are typically performed under arc welding conditions on thin section (3 mm) specimens. While these testing methodologies have provided a wealth of knowledge on solidification cracking, they are rather limited to specific process conditions, stress

---

states, and alloy systems. As a result, the susceptibility of an alloy to solidification cracking might vary significantly when subjected to different welding conditions or with changes in composition that will impact the solidification path.

Laser welding processes, particularly those performed at high powers, can impact the susceptibility of specific alloys to solidification cracking. Deep penetration laser welding processes performed at high laser powers, typically in excess of 5 kW, produce unique high aspect ratio weld profiles far different than those observed in arc welding processes. The thermal histories and solidification conditions can significantly vary with location, particularly with changes in weld depth [14], creating conditions which can enhance the susceptibility to defect formation in alloys which are readily weldable under traditional arc welding conditions [15,16]. During the deep penetration laser welding of a creep-resistant nickel alloy (Inconel 740H), for example, horizontal solidification cracking was consistently observed across the width of the fusion zones at depths between 70% and 80% of the overall weld depths [10]. These defects differed from the vertical centerline cracks typically attributed to solidification cracking in the relatively shallow weld pools produced under arc welding conditions [17–19]. By contrast, no such cracking was observed in Inconel 690 under similar deep penetration laser welding conditions [14].

This unique solidification cracking observed during deep penetration laser welding of these nickel base alloys arises from the combined effects of alloy composition, processing conditions, and stress state. Given the complexity of these interactions, the use of experimental or characterization techniques alone is inadequate for identifying the mechanisms driving the formation of these horizontal cracks. By integrating well-tested heat transfer and fluid flow and thermo-mechanical models, the complex thermal histories, solidification conditions, and the resulting stress states experienced across the entire weld geometry in both Inconel 740H and Inconel 690 were captured. Locations where the critical strain rate and tensile stresses co-existed were then identified using these modeling results and matched those where horizontal cracking was observed in Inconel 740H welds. On the other hand, no similar conditions were predicted nor was horizontal cracking observed in the Inconel 690 welds across all power levels.

Methods

A series of autogenous laser welds were fabricated on 12.7 mm thick Inconel 740H and Inconel 690 plates using an IPG Photonics[°1] YLR-12000-L ytterbium fiber laser delivered through a custom robotic welding system, with fiber diameter of 200 μm, collimating focal distance of 150 mm, and focusing distance of 600 mm. Individual welds approximately 50 mm in length were fabricated at laser powers ranging between 2.5 and 10 kW at a travel speed of 12.7 mm/s with a beam diameter in the sharp focus condition of 1.04 mm, Rayleigh length of 29.4 mm, divergence angle of 34.2 mrad, resulting in a beam parameter produce of 8.9 mm × mrad, which were confirmed through measurements using a Primes[°] Focus Monitor.

Transverse cross-sections were then extracted at locations approximately 10, 20, and 30 mm from the beginning of the weld in each sample and prepared using standard metallographic techniques to a final polishing step with a 1 μm diamond slurry. To reveal the weld cross-section, electrolytic etching was then performed using a Lucas solution (50 mL lactic acid + 3 g oxalic acid + 150 mL HCl) at a potential of 4 V for several seconds until the fusion zone profile was revealed. Optical microscopy techniques were then used to capture high-resolution images with a Zeiss SmartZoom 5 digital microscope.[2] Images were then analyzed using ImageJ[3] software to measure the weld dimension on those three individual cross sections taken from each weld to obtain average values and standard deviations for the individual weld widths and depths.

Computational thermodynamic calculations were utilized with commercially available tools to evaluate the solidification characteristics of the two alloys. Using the reported compositions for each alloy listed in Table 1, Scheil solidification simulations were performed using Thermo-Calc[4] software with the TCNI8 Ni-alloys database. The fraction of solid (fs) as a function of temperature during solidification and the formation sequence for different phases were obtained and analyzed for both alloys.

After examining the role of composition on the solidification behaviors of both alloys, a well-tested steady-state keyhole mode laser welding process model was then used to calculate the thermal histories experienced across the weldment [10]. This modeling approach couples a well-tested keyhole model with a three-dimensional heat transfer and fluid flow model, which solves the equations of mass, momentum, and energy in three-dimensions to calculate temperature and fluid flow fields across the weldment [20–22]. The keyhole profile is calculated first using a point-by-point heat balance at the keyhole wall, which is defined by the boiling temperature of the alloy. The calculated keyhole profile and the heat flux were then integrated into a heat

Table 1. Summary of composition, thermophysical properties, and weld dimensions of the two nickel alloys.

Alloys	Inconel 690		Inconel 740H	
	Composition (wt. %)			
Ni	Balance		Balance	
Cr	29.6		24.6	
Co	0		20.3	
Fe	9.7		0.2	
Nb	0		1.49	
Mo	0		0.05	
Mn	0.2		0.24	
Al	0		1.4	
Ti	0		1.5	
Si	0.08		0.1	
C	0.03		0.03	
Cu	0		0.02	
	Thermophysical Properties			
Density (kg/m^3)	8200		8200	
Dynamic viscosity (kg/ms) ♠	0.0075		0.007	
Solidus temperature (K)	1587		1425	
Liquidus temperature (K)	1664		1669	
Boiling temperature (K)	3084		3063	
Latent heat of fusion (J/kg)	2.26×10^5		2.82×10^5	
Specific heat (J/kgK)	$0.1T + 376$		$10^{-3}T^2 + 0.4T + 298$	
Thermal conductivity (W/mK)	$0.013T + 9.67$		$0.013T + 9.18$	
dγ/dT (N/mK)♣	-0.22×10^{-3}		-0.33×10^{-3}	
Laser absorptivity	0.2		0.2	
	Weld Dimensions			
Weld Depth (mm)	Experiment	Simulation	Experiment	Simulation
2.5 kW	3.7 ± 0.1	3.1	3.5 ± 0.1	3.1
5 kW	6.5 ± 0.1	5.8	6.2 ± 0.1	5.9
7.5 kW	8.3 ± 0.1	7.6	7.8 ± 0.2	7.8
10 kW	9.8 ± 0.1	9.1	9.5 ± 0.3	9.2
Weld Width (mm)				
2.5 kW	3.7 ± 0.2	3.1	3.8 ± 0.2	3.8
5 kW	5.0 ± 0.4	5.2	5.1 ± 0.1	5.6
7.5 kW	7.1 ± 0.1	6.7	6.7 ± 0.4	7.1
10 kW	8.8 ± 0.1	7.7	8.2 ± 0.1	8.8

♠The viscosity is at liquidus temperature.
♣γ is the surface tension.

transfer and fluid flow model to calculate the weld pool profile and corresponding thermal histories. In order to improve the accuracy and fidelity of these simulations, temperature- and composition-dependent thermophysical properties of the two nickel alloys used in these simulations were calculated using JMatPro[5] for the reported compositions of each alloy and provided in Table 1.

Since the output obtained from the model is comprised of the temperature at each location, additional manipulation of the data is required to obtain parameters specific to solidification. For example, the temperature gradients (G) were calculated by dividing the difference between the liquidus and solidus temperatures by the length of the mushy zone, and solidification rates (R) were determined by multiplying the welding speed and the local solidification direction [14]. Dendrite growth at any point on the solidification front follows this direction, which is approximately the principal heat flow direction and is normal to the solidification surface defined by liquidus temperature [23].

In order to calculate the resulting stress states surrounding the weld, the simulated temperature fields

from the heat transfer and fluid flow model were imported to a commercial finite element analysis model in Abaqus®.[6] Transfer of the temperature data was performed through the analytical mapped fields function in Abaqus using a point cloud file, and the temperature values on the nodes for the finite element model were defined by an inverse distance weighted method using the surrounding source points [24], as shown in Figure 1.

The calculation domain in the finite element model was 80 mm by 20 mm in the X and Y directions and 12.7 mm in the Z-direction, with the XZ plane used as a plane of symmetry and the XY plane, which represents the top surface of the weld, defined as a freely deformable surface. Mesh sizes were set at values between 200 μm and 500 μm, with finer meshes located inside and coarser meshes placed outside the molten pool. Since much finer meshes were used in the temperature (1,600,788 elements) than the stress (77,520 elements) calculations, a minimal error in the mapped temperature field is expected. No displacement or rotation is allowed on the four planes restrained by the surrounding base metal. In the model, the weld pool
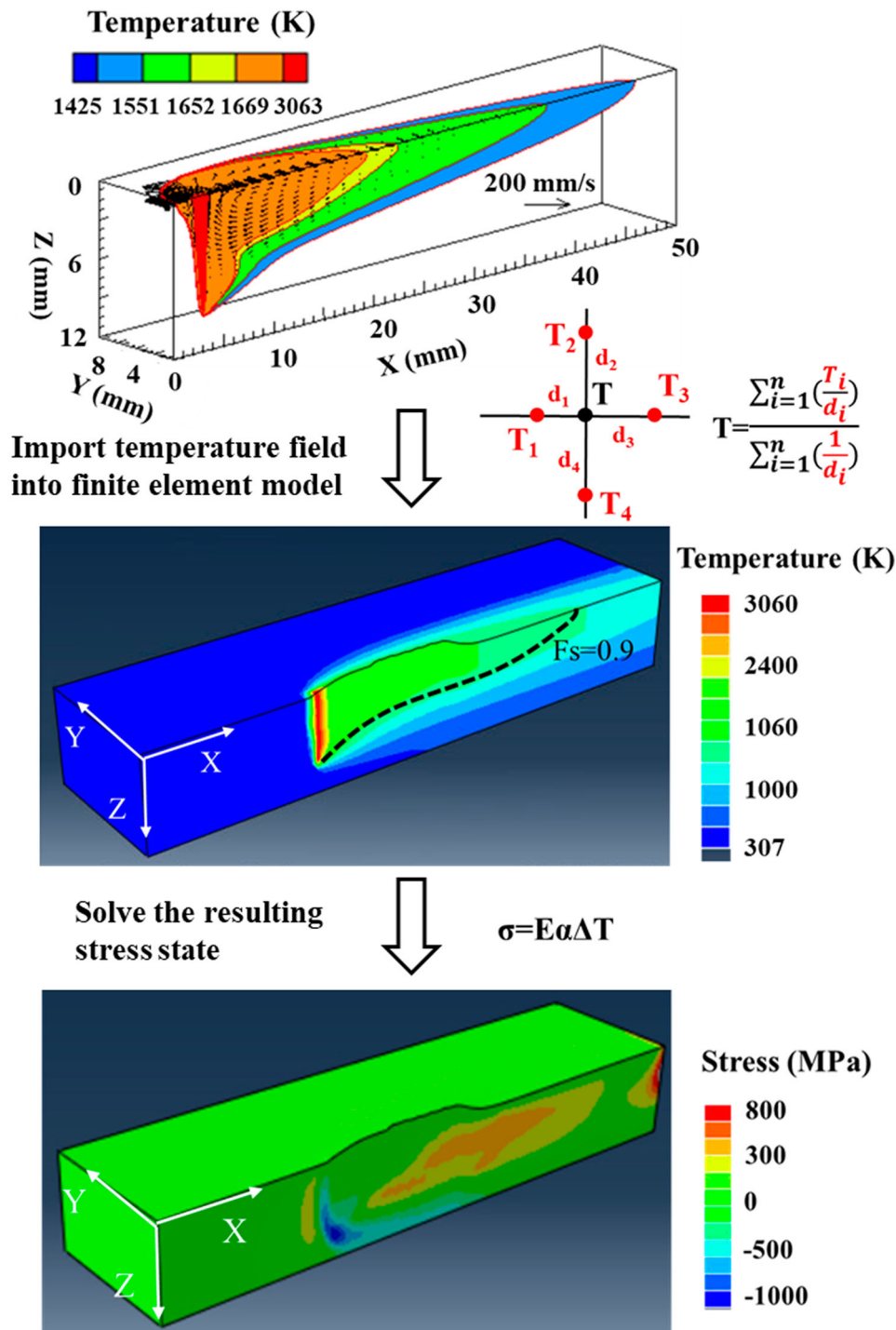
Figure 1. Schematic diagrams highlighting the procedures used for importing the temperature fields from the heat transfer and fluid flow model as a point cloud to the finite element model. The temperature T on a node in the finite element model was determined by the inverse distance weighted method using the surrounding source points, and the stress field was then solved according to the changes in the temperature field.

moved for around 1.2 s at a welding speed of 12.7 mm/s with an average time step size of 0.008 s. Calculated stresses and strain rates were then extracted at a corresponding time of 0.6 s along the plane of symmetry at locations where the fraction of solid (fs) was 0.9. The sensitivity of the calculation to the domain size and the average time step size was verified, and the results are summarized in Appendix. These results indicated that the calculation is not significantly affected.

Temperature-dependent mechanical properties of the alloys were obtained from manufacturer sources [25,26] to improve the accuracy of these calculations, which are shown in Figure 2. The values for Young's modulus and yield strength followed expected trends in the solid phase with increasing temperatures. Perfect plasticity without work hardening was assumed and considered to be reasonable since hardening at high temperatures is limited due to rapid dislocation motion

[27]. Although neglecting the work hardening effect might underestimate the stress levels, the tension to compression transition point is more critical in capturing the cracking locations than the absolute stress values away from the weld pool. After transformation to the liquid, both Young's modulus and yield strength were assumed to be 3% of the values at room temperature [28,29]. While thermal expansion with heating in the solid phase follows a generally linear trend, volumetric shrinkage during solidification becomes more complex and includes contributions from both thermal and solidification shrinkage. For a similar Ni-base alloy [30], this volumetric shrinkage can reach a level of approximately 1.64%, which results in a linear shrinkage of 0.55% by assuming that shrinkage is equal in all directions. In order to accommodate these differences, the coefficient of expansion between liquidus and solidus temperatures was assumed to vary linearly over the solidification temperature range.

Results and discussion

Deep penetration laser welding of Inconel 690 and Inconel 740H at high laser powers produces weld pool cross sections with shapes typical of keyhole mode laser welding, as shown in Figure 3. Increases in the laser power at a single travel speed (12.7 mm/sec) increased the weld width and depth for both alloys, which is summarized in greater detail in Table 1. Even though the alloy compositions vary, the measured weld depths and widths displayed strikingly similar values and trends across laser powers between 2.5 and 10 kW. For example, differences in weld width and depth typically fall below 5% of the measured width and depth and in many cases fall within the standard deviations.

Weld pool dimensions for both alloys were also successfully simulated using the well-tested heat transfer and fluid flow model and provided good agreement with the measured cross sections. Differences in the solidus temperature of the two alloys, which varied by nearly 162 K, led to significant changes in the solidification temperature range, with the Inconel 740H alloy displaying a solidification range on the order of 244 K, while that for the Inconel 690 alloy was only 77 K. Even with this difference in solidification range, the simulated weld dimensions, summarized in Table 1, were in good agreement with the experimental observations and generally fell within 10% of the experimental values.

While the weld pool cross sections display similar sizes and shapes, there is a prominent horizontal crack that appears across the fusion zone of the Inconel 740H welds produced at laser powers of 5 kW and above. This type of cracking in the Inconel 740H alloy has been connected with solidification cracking mechanisms [10], but no similar cracks were observed in the Inconel 690 welds, indicating that the differences in composition affected the cracking susceptibility. In order to confirm these differences, the solidification pathway, which is a primary indicator of the susceptibility of the alloy to solidification cracking, was calculated for each alloy using Scheil-Gulliver methods, and these pathways are shown in Figure 4. The much larger solidification temperature range for Inconel 740H (244 K) than Inconel 690 (77 K) is clearly shown in Figure 4(a). Across the solidification range, the changes in the calculated fraction of solid values can also capture the formation of different phases. It is clear that the Inconel 690 alloy has not only a small solidification temperature range but also solidifies as a single γ phase that persists through the terminal stages of solidification. On the other hand, the Inconel 740H alloy undergoes several additional phase transformations after the initial formation of the γ phase, ending in the formation of Laves phases at the terminal stages of solidification.

The susceptibility of an alloy to solidification cracking can also be connected to the slope of the solidification curve $(dT/d(fs^{1/2}))$ at these terminal stages of solidification (near $fs^{1/2} = 1$). Changes in the slope of the curve can capture the ability of the liquid to flow into regions between adjacent grains [2]. Differences between the two alloys are evident in Figure 4(b), with the slope of the curve for Inconel 690 having a value of 1010 K and being nearly half that of Inconel 740H, which displays a value of 2597 K. This higher value for Inconel 740H indicated that the remaining liquid at the terminal stage of solidification is more difficult to feed into the adjacent grains, resulting in higher solidification cracking susceptibility than Inconel 690.

Even though these criteria provide a means for evaluating the solidification cracking susceptibility for the two alloys, they do not capture how welding conditions can drive solidification cracking. For example, solidification cracking has not been observed during arc or low-power laser welding of Inconel 740H [10,15,16]. This cracking only appeared when welding was performed at laser powers of 5 kW and above, as shown in Figure 3. Changes in processing conditions, such as the laser power and travel speed, have distinct effects on both the shape of the pool as well as the corresponding solidification parameters. These changes are particularly prominent in the longitudinal views of the calculated liquidus and solidus isotherms, which are shown in Figure 5(a) for a laser power of 2.5 kW and in Figure 5(b) for a laser power of 7.5 kW.

Differences in the calculated solidification rate (R) and temperature gradient (G) values across the depth of these calculated fusion zones for these two laser powers in Inconel 740H are also captured in Figure 5(a) and (b). The temperature gradients generally increased with increasing depth at both laser powers, corresponding with a simultaneous decrease in the length of the mushy zone.
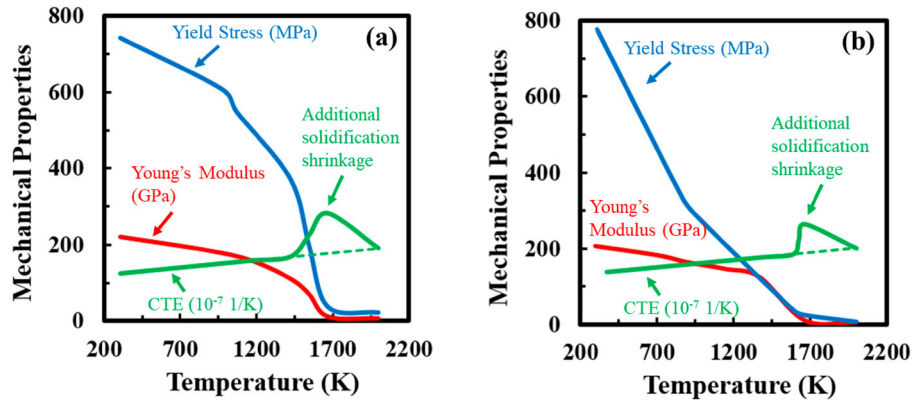
Figure 2. Plots showing the temperature dependent material properties of (a) Inconel 740H and (b) Inconel 690.
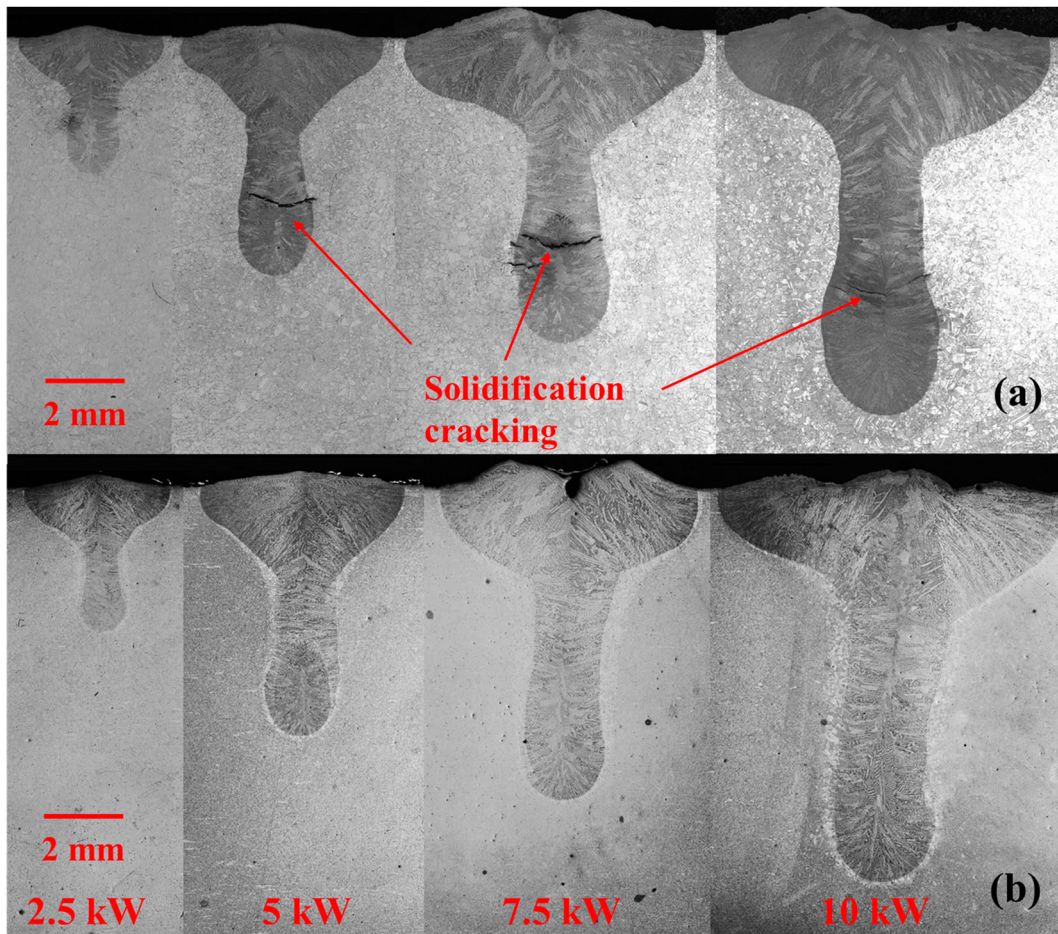

Figure 3. Representative cross section images of (a) Inconel 740H and (b) Inconel 690 under different laser powers.

On the other hand, the solidification rate displayed a series of complex variations across the weld depth, primarily driven by spatial variations in the solidification directions along the fusion zone/mushy zone boundary, which can be defined at the liquidus temperature. At a laser power of 2.5 kW, as shown in Figure 5(a), the solidification rate reached a peak value of approximately 10.9 mm/s at the bottom of the weld pool. Increasing the laser power to 7.5 kW, as shown in Figure 5(b), led to the formation of a nearly vertical solidification front where the solidification direction matched the welding direction and displayed solidification rates nearly identical to the travel speed (12.7 mm/s). When compared with the laser weld produced at the same 7.5 kW power in Inconel 690 welds, as shown in Figure 5(c), there are several notable differences. In particular, the solidification front observed in the Inconel 690 weld was not nearly as vertical near the bottom of the weld pool, and the peak solidification rates at these depths were slightly lower, reaching a value of approximately 11.3 mm/s.

These thermal and solidification conditions for the different alloys and processing conditions, in turn, affected the corresponding longitudinal (σ_x), transverse (σ_y), and through-thickness (σ_z) stress states across the mushy zone. Calculations of the strain rate
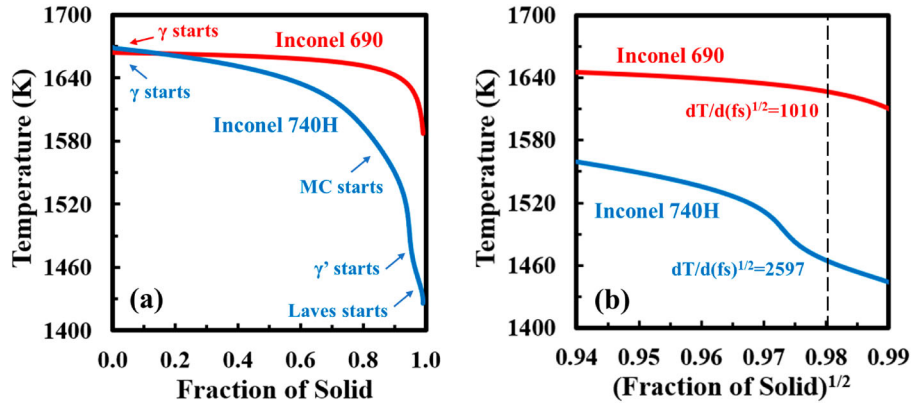
Figure 4. Comparison of solidification path for two nickel alloys showing the (a) solidification temperature range and the secondary phases and the (b) $fs^{1/2}$ vs T curves. Values of $dT/d(fs^{1/2})$ were calculated at an $fs^{1/2}$ value of 0.98.
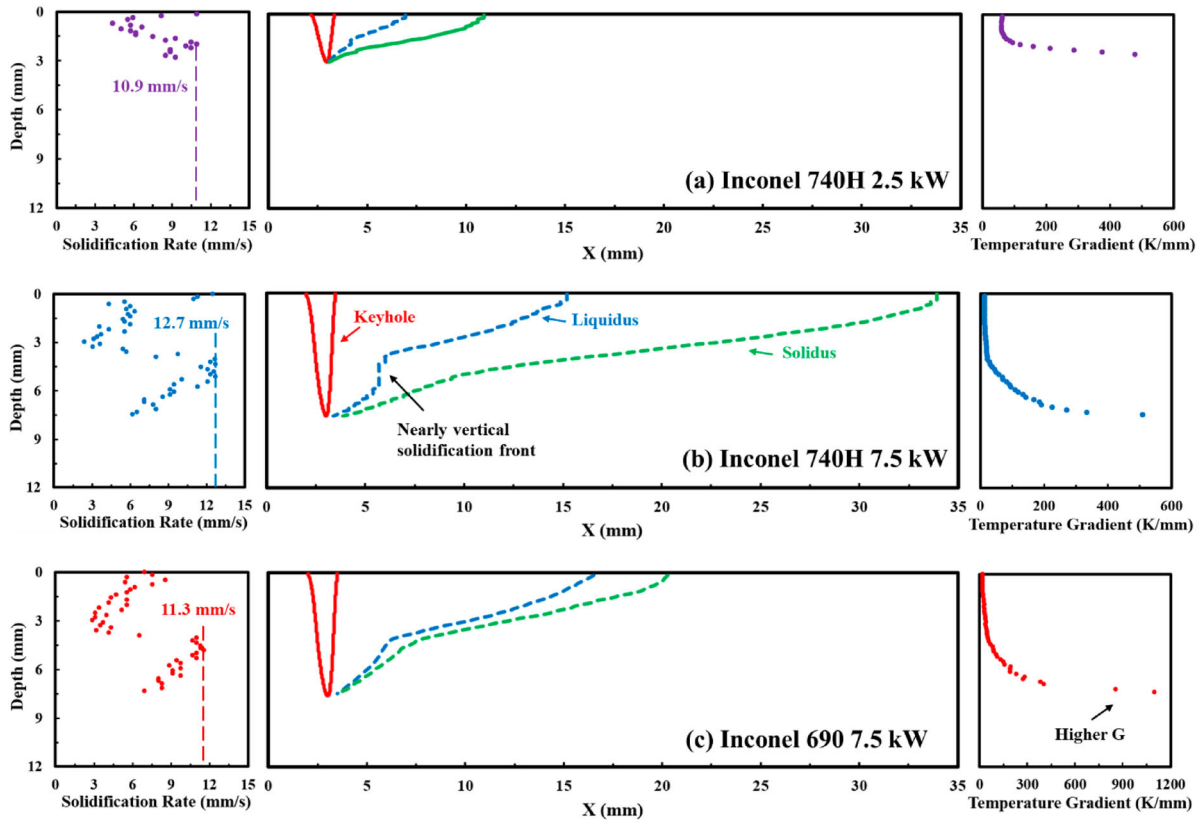
Figure 5. The calculated profiles of the solidification front and its impact on the solidification rate and temperature gradient for (a) Inconel 740H weld produced at a laser power of 2.5 kW, (b) Inconel 740H weld produced at a laser power of 7.5 kW, and (c) Inconel 690 weld produced at a laser power of 7.5 kW.

and stress values were then made, as shown schematically in Figure 6(a), at locations along the weld length at depths where an fs value of 0.9 was obtained. Strain rates and stress levels across the longitudinal, transverse, and vertical orientations for a laser weld made on Inconel 740H at a laser power of 7.5 kW are shown in Figure 6(b) and (c), respectively. Similar trends in the strain rate and stress levels were observed across the three directions, but the lowest tensile stress and negative strain rate values were observed in the transverse direction across all depths. Since transverse shrinkage had the smallest contribution to the overall stress levels observed at each location, horizontal cracking was

primarily driven by the strain rates and stresses in the vertical and longitudinal directions.

Spatial distributions of the calculated vertical stresses for laser welds fabricated at a laser power of 7.5 kW were shown in Figure 7(a) and (b) for Inconel 740H and Inconel 690, respectively. The magnitude of the vertical stresses developed across the trailing edge of the solidifying weld metal during laser welding of Inconel 740H was much higher than that in Inconel 690, particularly in the region of the vertical solidification front identified in Figure 5(b).

The effective stresses, normal to the solidification direction (σ_n), which combined the effect of σ_x, σ_y, and
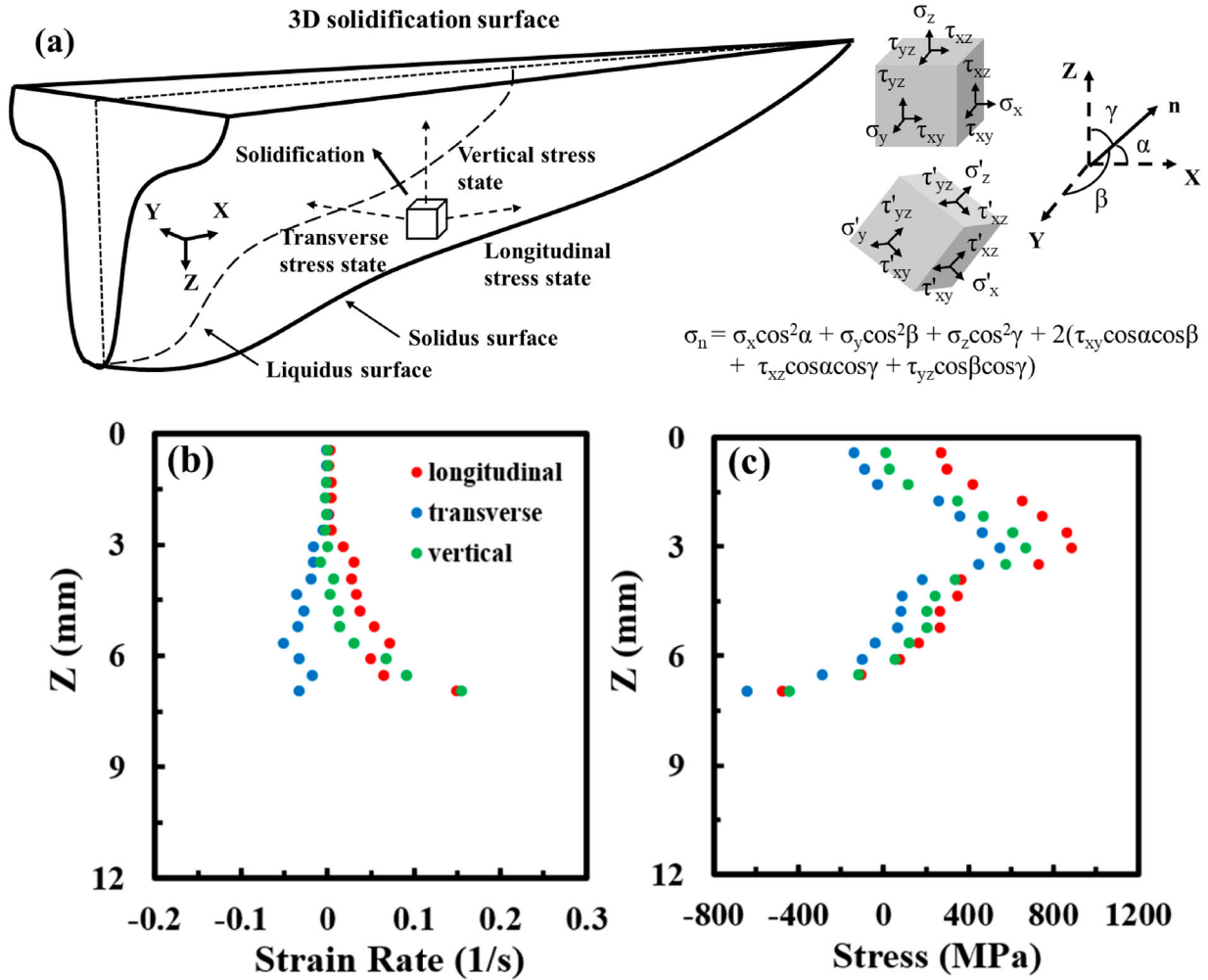
Figure 6. (a) Schematic diagram showing the extraction of stress states along the longitudinal, transverse, and vertical direction and the three-dimensional stress transformation rules, where σ_n is normal to the grain growth direction. A comparison of the (b) strain rate and (c) stress values in the three directions for Inconel 740H under a laser power of 7.5 kW is also shown.

σ_z, are better indicators of the conditions that can lead to cracking and were calculated using the relationship shown in Figure 6(a). Variations in these effective strain rates and stresses normal to the solidification direction were then obtained along the weld depth for the two alloys and shown in Figure 7(c) and (d), respectively. The strain rate generally increased with the weld depth in a manner similar to the temperature gradient across these same locations. Strain rates between 0.011 and 0.019 s^{-1} are necessary to initiate solidification cracking for nickel alloys [5], and a critical strain rate of 0.019 s^{-1} is used as the threshold for the onset of solidification cracking. Owing to the uncertainty in the calculation, the strain rate needs to be considerably higher than this value to ensure the critical strain rate of the nickel alloys is attained. As shown in Figure 7(c) and Figure 7(d) for laser welds made at a power level of 7.5 kW, this critical strain rate level was considerably exceeded below approximate depths of 5.2 and 3.9 mm for Inconel 740H and Inconel 690, respectively.

Since cracking does not occur under a compressive stress state, a tensile stress state, in combination with a strain rate exceeding this critical level, is required

for crack propagation. The transition from a tensile to a compressive stress state is observed at a depth of approximately 6.1 mm in the Inconel 740H weld and 3.5 mm for the Inconel 690 weld. For welds made at a laser power of 7.5 kW in Inconel 740H, strain rates considerably higher than 0.019 s^{-1} along with a corresponding tensile stress state were observed over a 0.9 mm range at depths corresponding to the location where cracking was observed. In the Inconel 690 weld, the critical strain rate and tensile stress levels required to promote cracking are not obtained at any location across the weld depth, as shown in Figure 7(d).

These calculations were then extended to other processing conditions in which cracking was observed in the Inconel 740H welds. Across these different power levels, locations at which horizontal cracking was observed corresponded with those where the critical strain rate and tensile stress levels were predicted. For example, the simulations were able to closely predict the locations where cracking was observed as laser power levels increased from 5 to 10 kW, as shown in Figure 7(e). Expanding these calculations further, a range of crack susceptible regions was identified, with
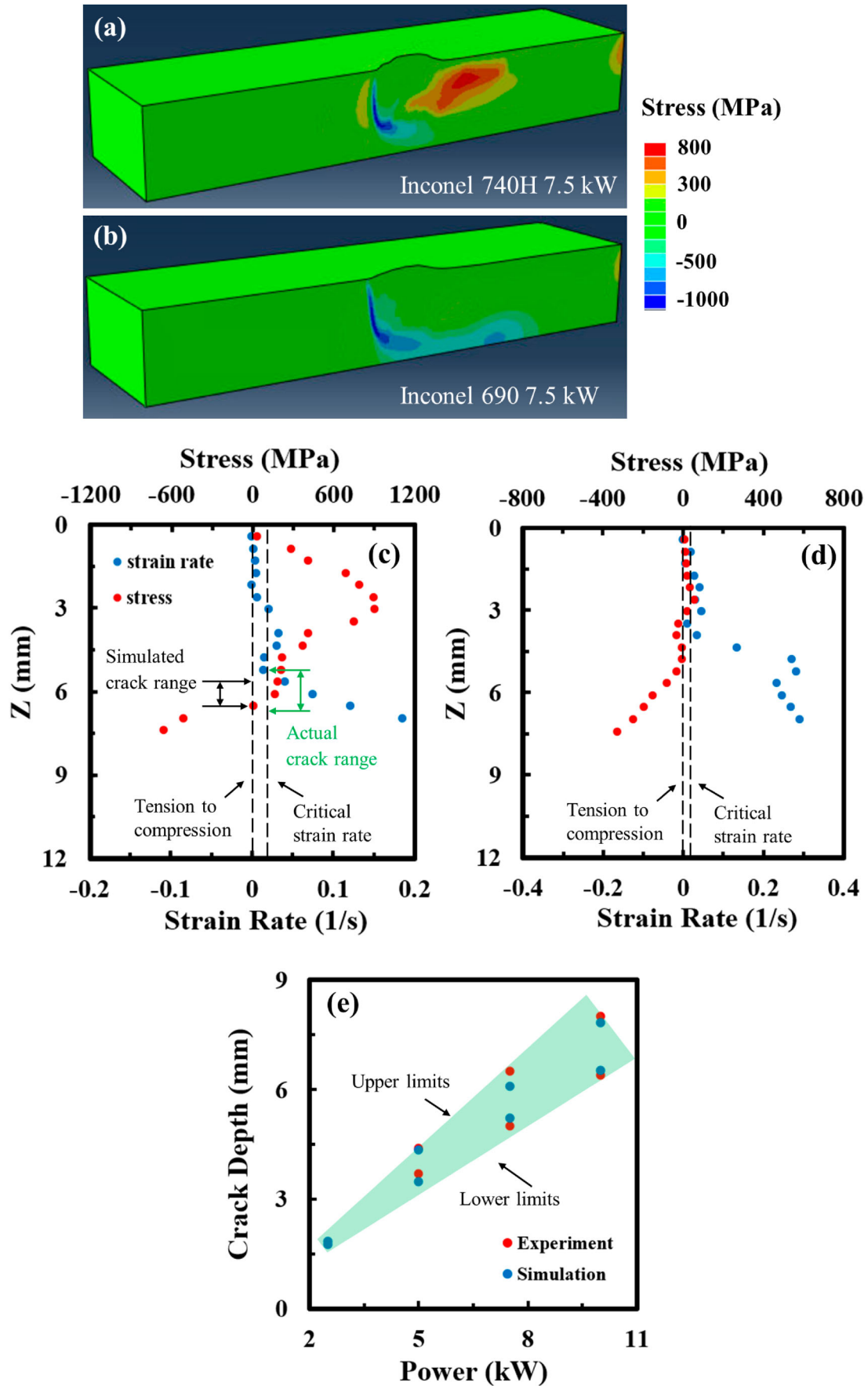
Figure 7. Plots showing the calculated vertical stress distribution of (a) Inconel 740H and (b) Inconel 690 welds produced at a laser power of 7.5 kW. The variation of effective stress and strain rate values along weld depth at fs = 0.9 were shown for (c) Inconel 740H and (d) Inconel 690 under laser power of 7.5 kW and the welding speed of 12.7 mm/s. (e) The locations where horizontal cracking is predicted to occur are highlighted by comparing experimentally measured and numerically calculated crack depths defined by the critical strain rate (lower limits) and the tension to compression transition point (upper limits) for Inconel 740H under different laser powers.

the lower limit in depth defined by the critical strain rate and the upper limit by the tension to the compression transition point. As the laser powers increased, these regions where the critical strain rate and tensile stresses indicated crack susceptibility covered larger depth ranges within the welds.

Summary and conclusions

Deep penetration laser welding of Inconel 740H and Inconel 690 was performed across a range of laser powers from 2.5 to 10 kW. Even though the two alloys displayed similar transverse cross sections across these different processing conditions, there were prominent differences in their susceptibility to fusion zone cracking. While Inconel 690 welds displayed no cracking across all processing conditions, Inconel 740H welds experienced horizontal cracking across the fusion zone at locations between 70% and 80% of the weld depth at laser powers of 5 kW and above. In order to capture the complex interactions between composition and processing leading to the appearance of cracking, well-tested heat transfer and fluid flow and thermo-mechanical models were integrated to calculate thermal histories, solidification conditions, and the resulting stresses and strain rates across the solidifying mushy zone. These unique calculations provide a means for predicting horizontal cracking susceptibility and location by identifying the simultaneous appearance of critical strain rate and tensile stress levels across different laser powers in Inconel 740H high-power welds. Additional details and conclusions are provided below:

- Similar dimensions and profiles were observed in the transverse cross sections extracted from Inconel 690 and Inconel 740H high-power laser welds across a range of laser powers. Even though both alloys had similar thermophysical properties, Inconel 740H displayed 167 K larger solidification temperature range and higher solidification cracking susceptibility than Inconel 690.
- Increased weld lengths and elongated mushy zones were observed in Inconel 740H along the welding direction in the three-dimensional weld pool profiles obtained from the heat transfer and fluid flow models. At laser powers greater than 5 kW, which corresponded with the appearance of horizontal cracks between 70% and 80% of the weld depth, the solidification front took on a near-vertical profile in these regions, where higher local solidification rates were also observed.
- The calculated thermal histories and solidification conditions were then used to model stresses and strain rates across the welds in both alloys. Spatial variations in stress states were observed across the welds, with strain rates increasing across the weld depth and the stresses transforming from tensile to compressive states near the weld root.
- Horizontal cracking in the Inconel 740H welds produced at powers in excess of 5 kW corresponded to regions where a critical strain rate of $0.019 \, \text{s}^{-1}$ and tensile stresses were simultaneously observed normal to the solidification direction. This condition was observed across these laser powers and consistently predicted locations along the weld depth where this horizontal cracking was observed.
- In the Inconel 690 welds and in low power Inconel 740H laser welds, these combined tensile strain rate and stress levels were not achieved, leading to the elimination of these horizontal cracks.

Disclosure statement

No potential conflict of interest was reported by the author(s).

ORCID

T. A. Palmer http://orcid.org/0000-0001-9573-3319

References

[1] Sheikhi M, Malek Ghaini F, Assadi H. Prediction of solidification cracking in pulsed laser welding of 2024 aluminum alloy. Acta Mater. 2015;82:491–502.
[2] Kou S. A criterion for cracking during solidification. Acta Mater. 2015;88:366–374.
[3] Tokita S, Kadoi K, Kanno Y, et al. Microstructural evolution and solidification cracking susceptibility of grain boundary engineered fully austenitic stainless steel. Weld World. 2020;64(4):593–600.
[4] Aucott L, Huang D, Dong HB, et al. Initiation and growth kinetics of solidification cracking during welding of steel. Sci Rep. 2017;7:1–10.
[5] Xia C, Kou S. Evaluating susceptibility of Ni-base alloys to solidification cracking by transverse-motion weldability test. Sci Technol Weld Join. 2020;25(8):690–697.
[6] Dupont JN, Robino C V, Marder AR. Solidification and weldability of Nb-bearing superalloys. Weld J. 1998;77(10):417–431.

[7] Clyne TW, Wolf M, Kurz W. The effect of melt composition on solidification cracking of steel, with particular reference to continuous casting. Metall Trans B. 1982;13(2):259–266.

[8] Rappaz M, Drezet JM, Gremaud M. A new hot-tearing criterion. Metall Mater Trans A Phys Metall Mater Sci. 1999;30(2):449–455.

[9] Coniglio N, Cross CE. Initiation and growth mechanisms for weld solidification cracking. Int Mater Rev. 2013;58(7):375–397.

[10] Mondal B, Gao M, Palmer TA, et al. Solidification cracking of a nickel alloy during high-power keyhole mode laser welding. J Mater Process Technol. 2022;305(3):117576.

[11] Mondal B, Mukherjee T, DebRoy T. Crack free metal printing using physics informed machine learning. Acta Mater. 2022;226:117612.

[12] Coniglio N, Cross CE. Mechanisms for solidification crack initiation and growth in aluminum welding. Metall Mater Trans A Phys Metall Mater Sci. 2009;40(11):2718–2728.

[13] Soysal SK T. A simple test for solidification cracking susceptibility and filler metal effect. Weld J. 2017;96(10):389–401.

[14] Blecher JJ, Palmer TA, Debroy T. Solidification map of a nickel-base alloy. Metall Mater Trans A. 2014;45(4): 2142–2151.

[15] Bechetti DH, DuPont JN, de Barbadillo JJ, et al. Microstructural evolution of INCONEL* alloy 740H* fusion welds during creep. Metall Mater Trans A Phys Metall Mater Sci. 2015;46(2):739–755.

[16] de Barbadillo JJ. INCONEL alloy 740H. Mater Ultra-Supercritical Adv Ultra-Supercritical Power Plants. 2017;740:469–510.

[17] Liu J, Zeng P, Wu Y, et al. Determination of tensile strain causing solidification cracking in welding. Sci Technol Weld Join. 2020;25(5):431–437.

[18] Chen S, Ye XX, Tsang DKL, et al. Welding solidification cracking susceptibility and behavior of a Ni-28W-6Cr alloy. J Mater Sci Technol. 2019;35(1):29–35.

[19] Niel A, Bordreuil C, Deschaux-Beaume F, et al. Modelling hot cracking in 6061 aluminium alloy weld metal with microstructure based criterion. Sci Technol Weld Join. 2013;18(2):154–160.

[20] Rai R, Elmer JW, Palmer TA, et al. Heat transfer and fluid flow during keyhole mode laser welding of tantalum, Ti-6Al-4 V, 304L stainless steel and vanadium. J Phys D Appl Phys. 2007;40(18):5753–5766.

[21] Rai R, Roy GG, Debroy T. A computationally efficient model of convective heat transfer and solidification characteristics during keyhole mode laser welding. J Appl Phys. 2007;101(5):1–11.

[22] Rai R, Kelly SM, Martukanitz RP, et al. A convective heat-transfer model for partial and full penetration keyhole mode laser welding of a structural steel. Metall Mater Trans A Phys Metall Mater Sci. 2008;39(1):98–112.

[23] Wei HL, Mazumder J, DebRoy T. Evolution of solidification texture during additive manufacturing. Sci Rep. 2015;5:1–7.

[24] Smith M. Abaqus/CAE User's Manual, Version 6.12. Dassault Systemes Simulia Corp., Providence, RI, USA. 2012.

[25] Specialmetals. https://www.specialmetals.com/documents/technical-bulletins/inconel/inconel-alloy-740h.pdf . May 13th 2022.

[26] Specialmetals. https://www.specialmetals.com/documents/technical-bulletins/inconel/inconel-alloy-690.pdf. May 13th 2022.

[27] Semiatin SL, Mahaffey DW, Tung DJ, et al. A comparison of the plastic-flow response of a powder-metallurgy nickel-base superalloy under nominally-isothermal and transient-heating hot-working conditions. Metall Mater Trans A Phys Metall Mater Sci. 2017;48(4):1864–1879.

[28] Kitano H, Tsujii M, Kusano M, et al. Effect of plastic strain on the solidification cracking of Hastelloy-X in the selective laser melting process. Addit Manuf. 2021;37:101742.

[29] Mukherjee T, Zhang W, DebRoy T. An improved prediction of residual stresses and distortion in additive manufacturing. Comput Mater Sci. 2017;126:360–372.

[30] Xiao F, Yang R, Fang L, et al. Solidification shrinkage of Ni-Cr alloys. Mater Sci Eng B Solid-State Mater Adv Technol. 2006;132(1–2):193–196.

Appendix

Sensitivity check for thermal stress state calculation

In the stress simulation in Abaqus, the time step size and the domain size can potentially impact the calculated results, and the sensitivity of the calculations to these variables needs to be checked to ensure the accuracy of the calculated results. In the reference case, the average time step size was 0.008 s and the calculation domain size was 80 mm by 20 mm by 12.7 mm. In the 'fine steps' case, the average time step size was reduced to 0.005 s and the calculation domain size remained the same as in the reference case. In the 'large domain' case, the average time step was 0.008 s while the domain size was 120 mm by 30 mm by 12.7 mm. These three cases were simulated with laser power of 10 kW and welding speed of 12.7 mm/s, and the data were extracted at fs = 0.9 at three depths (d), 6.1, 7.0, and 8.3 mm, which represented depths above the cracking region, within the cracking region, and below the cracking region, respectively.

Figure A1 showed the calculated effective strain rate and stress (σ_n) that are normal to the solidification direction at a series of time frames for the three cases. It can be seen that the calculated values are generally consistent at different time frames. On the other hand, even though small variations were observed when using different domain sizes and average time step sizes, the trends for the different depths remained the same. For example, at depth of 6.1 mm, the calculated strain rate values are all below the critical strain rate likely due to the low temperature gradient at this depth, indicating no crack can be initiated. At depth of 8.3 mm, the stress values are all negative, meaning this depth is in compression for all three cases. Owing to the same trend of strain rate and stress at different depths, the simulated crack depths in Figure 7(e) remains unchanged even using different domain size or time step size, which indicated that the calculation results are not significantly affected by these variables.
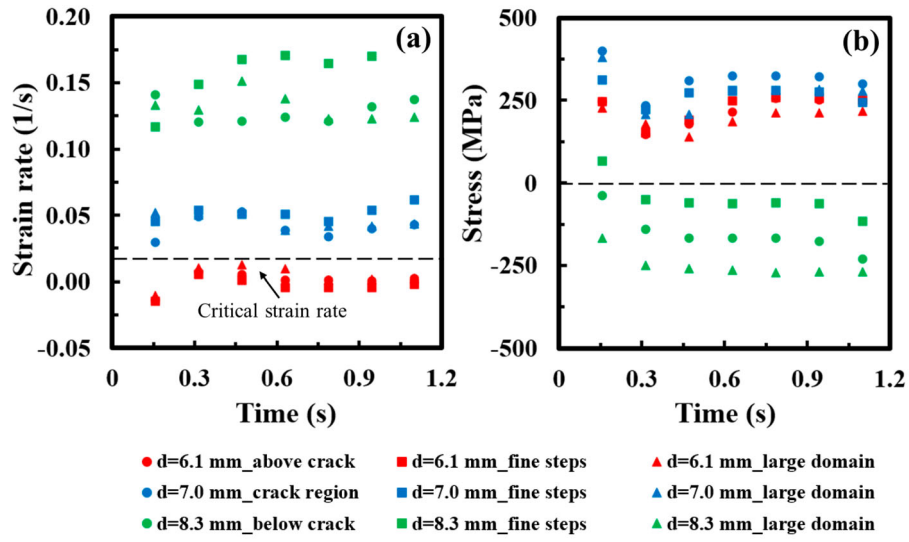
Figure A1. Calculation sensitivity check with respect to different time steps and domain sizes at three depths under laser power of 10 kW and welding speed of 12.7 mm/s.